Layer-by-Layer Construction of Hybrid Film Based on PEI Polymer and Preyssler-Type Polyoxometalates: Its Electrochemical and Quartz Crystal Microbalance Measurement

Athira Kuruly Rajan, Indherjith Sakthinathan, Séverine Renaudineau, Anna Proust, Timothy Mccormac

DOI: 10.1002/celc.202400102

Research Article

Layer-by-Layer Construction of Hybrid Film Based on PEI Polymer and Preyssler-Type Polyoxometalates: Its Electrochemical and Quartz Crystal Microbalance Measurement

Athira Kuruly Rajan,[a] Indherjith Sakthinathan,[a] Séverine Renaudineau,[b] Anna Proust,[b] Timothy McCormac *[a]

[a] Electrochemistry Research Group, Department of Applied Science, Dundalk Institute of Technology, Dublin Road, Dundalk- A91K584, Ireland
E-Mail: tim.mccormac@dkit.ie

[b] Sorbonne Université, CNRS, IPCM, Université Pierre et Marie Curie, 4 place Jussieu, F- 75005 Paris, France

Employment of layer-by-layer technique for the immobilisation of Preyssler type polyoxometalate using polyethyleneimine polymer on a 4-mercaptobenzoic acid self-assembled gold electrode. Cyclic voltammetry and electrochemical impedance spectroscopy were used to characterise the electrochemical behaviour of the modified films. An in-situ electrochemical quartz crystal microbalance was employed for studying the solvation of electrolyte ions into film during potential switching.

In this work, Preyssler-type POM $(NH_4)_{14}[NaP_5W_{30}O_{110}].44H_2O$ ($NH_4P_5W_{30}$), has been synthesised and its electrochemical behaviour in solution was examined at the surface of glassy carbon (GC) and gold electrodes. Furthermore, multilayer assemblies of $NH_4P_5W_{30}$ POM were constructed onto the surfaces of GCE, gold electrode, and gold quartz electrode via the electrostatic Layer-by-Layer (LBL) technique employing polyethyleneimine as the cationic layer and POM as an anionic layer. Cyclic voltammetry, electrochemical impedance spectroscopy (EIS), and electrochemical quartz crystal microbalance measurements (EQCM) were used to monitor the LBL assembly as the $NH_4P_5W_{30}$ POM layer was being built. These techniques revealed significant differences in film growth. The multilayer film exhibited well-defined redox couples associated with POM's tungsten-oxo framework and showed surface-confined behaviour up to $100mVs^{-1}$ on both the GC and gold electrodes. The pH dependency and stability of the film were investigated. EIS demonstrated that when the POM layer was

the outer layer, the layers were less conductive, and resistance increased as the number of layers increased. In addition, the charge transfer resistance values (R_{ct}) for the layers were calculated. The solvation of ions into the film associated with POM redox activity was studied employing an in-situ EQCM.

Polyoxometalate
Preyssler
Layer by Layer
Polyethyleneimine
EQCM

1. Introduction

Polyoxometalates (POMs) are a significant class of inorganic metal oxide nanoclusters possessing a wide domain of structure and abundant elemental compositions.[1--3] POM's versatile properties, including stable redox states and the ability to undergo multi-electron redox processes with negligible structural changes, enable them to be employed across a large spectrum of applications, such as catalysis,[4] energy,[5] memory,[6] optics,[7] sensor,[8] magnetism[9] and bio-applications.[10] POM architectures are mostly formed by the condensation of oxygen atoms and early transition metals most commonly vanadium (V),[11] molybdenum (Mo)[12] tungsten (W),[13] and less commonly niobium (Nb)[14] and tantalum (Ta)[15] or a mixture of these elements in their higher oxidation states. In particular, tungsten oxide-based compounds are a promising candidate for various applications such as photoanodes,[16--18] energy storage devices,[19,20] electrocatalysis,[21] biomedical applications,[22] etc.

Preyssler is an interesting polyoxometalate with a doughnut shape formed by a circular arrangement of five PW_6O_{22} units derived from the Keggin anion $[PW_{12}O_{40}]^{3-}$.[23,24] The Preyssler POM was first reported by Preyssler in 1970, but Pope, Jeannin and co-workers resolved the structure using the X-ray diffraction technique 15years later.[25] The structure of the Preyssler anion is given in Figure1a.[26] The Preyssler POM can function as an inorganic

building linker due to its high oxygen content (30 terminal O atoms and 60μ_2<C->O atoms) and significant Bronsted acidity (14 acidic protons), which makes it easier to coordinate with metal ions[27--29] and organic moieties.[30,31] An interesting fact about Preyssler POM is its ability to encapsulate various cations such as Na^+, K^+, Ag^+, Ca^{2+}, Bi^{3+}, Y^{3+}, lanthanide, and actinide cations and their physiochemical properties are changed in accordance with the encapsulated cation.[32] The Preyssler POM has remarkable thermal stability.[33] Additionally, M.H. Alizadeh and colleagues studied the electrochemical behaviour of the $[NaP_5W_{30}O_{110}]^{14-}$ in solutions in the pH range of 0 to 12, which suggests that the Preyssler POM might be employed in all pH ranges.[34] To date, several Preyssler-based compounds have been successfully synthesised and exploited in various applications. H. Zhao *et al* synthesised two 2D Preyssler POM-based organic-inorganic hybrids for solid-state photoluminescence.[28] Non-enzymatic H_2O_2 sensors were constructed using Preyssler-type POM-based organic-inorganic hybrid materials and reported by H. Zhu *etal.*[31] Using the LBL approach, S. Liu *etal.* fabricated a Preyssler-type Eu-POM incorporated electrochromic device.[35] Whereas, S. Saneinezhad *et al* explored cellulose-functionalised Preyssler as a green catalyst for the in-situ synthesis of Pd nanoparticles.[36] The influence of counter ions on the electron transport properties at the nanoscale of P_5W_{30}-based molecular junctions for POM-based molecular devices were demonstrated by C. Huez *etal.*[37] The Preyssler anion is an electroactive water-soluble anionic cluster, that features a rich electrochemistry evidenced by its ability to accept electrons at low potentials.[38] Therefore, it is noteworthy for doing a systematic study of Preyssler POM in an immobilised state for a better understanding of their electrochemical behaviour.

The immobilisation route using the electrostatic process, namely the Layer-by-Layer (LBL) self-assembly, constitutes a simple and reliable method to build well-ordered redox-active architectures with excellent control of the film thickness and the surface coverage of the entrapped functionality. This method relies on the electrostatic LBL assembly of

positively and negatively charged polyionic compounds.[39-42] Multiple repetitions of the adsorption steps result in multilayer film with precisely controlled thickness and composition. For LBL deposition a plethora of materials can be taken including polymers,[35] nanoparticles,[43] proteins,[44] dyes,[45] enzymes,[46] graphene-based materials,[47] cationic linkers[48] and so on. The precise structure of each layer can be tuned with adsorption times, concentration, ionic strength, pH solvent concentration or temperature.[49]

Liu *etal.* adopted the LBL method for a detailed investigation of POM multilayer assembly concerning optical adsorption, fluorescence, and electrochemistry.[50] M. Jiang *etal.* used the LBL method followed by post photoreduction for the reduction of graphene oxide in multilayers to fabricate a multilayer film containing $K_{12.5}Na_{1.5}[NaP_5W_{30}O_{110}]$ POM, graphene oxide, and polyethyleneimine to investigate the electrocatalytic behaviour toward oxygen reduction and hydrogen evolution reactions.[51] From the literature survey, it was found that a detailed electrochemical study of the immobilised Preyssler POM has not been reported yet.

In this contribution, the successful immobilisation of Preyssler POM $(NH_4)_{14}[NaP_5W_{30}O_{110}].44H_2O$ ($NH_4P_5W_{30}$) on glassy carbon and gold electrode substrates using simple polyethyleneimine (PEI, Figure1b) as the cationic layer was achieved with the employment of the LBL method. The electrochemical properties of the films have been investigated using cyclic voltammetry (CV), electrochemical impedance spectroscopy (EIS) and electrochemical quartz crystal microbalance measurements (EQCM). EQCM measurements were performed with $NH_4P_5W_{30}$ POM-modified gold quartz crystal electrode to investigate the ion transfer phenomena. The rationale for conducting this research was to understand the electrochemical behaviours of immobilised $NH_4P_5W_{30}$ POM on various electrode surfaces. We believe that this strategy is suitable for the synthesis of stable nanoscale-based electrocatalysts for the hydrogen evolution reaction, oxygen reduction reaction, and many other applications.

Experimental

Materials

Potassium ferricyanide, potassium ferrocyanide, polyethyleneimine (PEI, MW ~75,000), 4-mercapto benzoic acid (MBA) and all other chemicals were purchased from Sigma -- Aldrich. Highly purified water with a resistivity of 18.2MΩcm (ELGA PURELAB Option-Q) was used for the preparation of the electrolyte and buffer solutions. The pure Preyssler type POM $(NH_4)_{14}[NaP_5W_{30}O_{110}].44H_2O$ ($NH_4P_5W_{30}$) was synthesised and characterised according to the literature.[52] The following buffer solutions have been employed for the electrochemical investigations: 0.1M Na_2SO_4 (pH 2--3), 0.1M Na_2SO_4 + 20mM CH_3COOH (pH3.5-5), 0.1M Na_2SO_4+20mM NaH_2PO_4 (pH5.5-7). The pH of the solutions was adjusted with either 0.1M NaOH or 0.1M H_2SO_4.

Apparatus and Instrumentation

All electrochemical experiments were performed with the CHI660C electrochemical workstation in a conventional three-electrode electrochemical cell using a glassy carbon electrode (3mm diameter, area 0.0707cm^2) /or gold electrode (2mm diameter, area 0.0314cm^2) electrode as the working electrode. Ag/AgCl (saturated KCl) and a platinum wire were the reference and auxiliary electrodes, respectively. The EQCM measurements were recorded using a CHI440a potentiostat connected to a QCM external oscillator box. 7.995MHz gold quartz crystal electrode is used as the working electrode for EQCM measurements. The AC impedance experiments were carried out in 1mM potassium ferricyanide and 1mM potassium ferrocyanide in 0.1M KCl solution with a frequency range of 0.01 to 10^6Hz with a voltage amplitude of 5mV.

Preparation of Working Electrodes

Electrodes Cleaning

Step 1: The electrodes were polished with 1.0, 0.3 and 0.05μm Al_2O_3 powders and sonicated in water for about a minute after the polishing step.

Step 2: After the mechanical polishing step, the electrode is electrochemically cleaned by cycling in 0.5M H_2SO_4 between 0 and 1.5V *vs* Ag/AgCl at a scan rate of 100mVs^{-1}.

Step 3: Finally, all the electrodes were washed with ethanol and then dried with a high-purity argon stream before use.

To clean the GC electrodes step 1 and 2 have been followed. The pretreatment of the gold electrode has been performed using steps 1, step 2 and step 3. The quartz crystal electrodes have been cleaned by steps 2 and 3.

Formation of Multilayer Film on GCE and Gold Electrode

GCE: After the polishing step, A multilayer film of $NH_4P_5W_{30}$ POM was built onto the GCE surface by the following steps: (1) immersion the precleaned GCE into a 2% PEI solution for 20 minutes; (2) Immerse the PEI modified GCE in 2mM $NH_4P_5W_{30}$ POM solution for 20 minutes. Wash the electrode gently with plenty of millipore water, washed with ethanol and dried under a slow nitrogen stream between each deposition step. Thus, one bilayer is fabricated onto GCE. Steps 1 to 2 were repeated n times for building n number of $(PEI/NH_4P_5W_{30})_n$ bilayers.

Gold electrode: Before following the above-mentioned steps, the gold electrode was pretreated with 1mM of MBA solution for 1hour and 30 minutes, then rinsed with ethanol and dried under the nitrogen stream for the MBA-modified gold electrode. The concentration of $NH_4P_5W_{30}$ POM dipping solution is taken as 5mM for improved adsorption.

Formation of Multilayer Film on Gold Quartz Electrode

The gold crystal electrodes were modified using the same technique used to create multilayer films on gold electrodes. After cleaning the gold quartz electrodes, the electrode was fitted into the

electrochemical cell and then filled with the desired solution for deposition. The cell is emptied and gently cleansed thrice with millipore water following the immersion period.

2. Results and Discussion

2.1. Voltammetric Behaviour of $NH_4P_5W_{30}$ in Aqueous pH 2 Buffer Solution

The solution electrochemical properties of the $NH_4P_5W_{30}$ POM at both GC and gold electrodes in a pH2 buffer solution were studied by using the CV technique. Figures3<figr3>a and 3b illustrate the resulting cyclic voltammograms of the $NH_4P_5W_{30}$ POM using GCE and gold electrodes respectively. Figure3<xfigr3>a shows three redox couples labelled as I/I', II/II' and III/III' with the mean peak potentials $E_{1/2}$, ($E_{1/2}$=(E_{pa}+E_{pc})/2) of -0.295, -0.420 and -0.590V *vs* Ag/AgCl respectively. These three redox couples are related to the tungsten-oxo (WO) centre as I/I' and II/II' represent two consecutive four electronic redox processes while redox couple III/III' represents multi-electronic redox process, $E_{1/2}$ values matched with the previous literature.[34,38] Meanwhile, only two WO redox couples labelled as I/I' and II/II' with E½ values -0.288V and -0.416V *vs* Ag/AgCl were observed on the gold electrode (Figure3b). Both redox couples are believed to be four electronic redox processes. The $NH_4P_5W_{30}$ POM's third redox couple obtained at GCE was not observed at the gold electrode because of the hydrogen evolution reaction overlap.

A scan rate study was performed with $NH_4P_5W_{30}$ POM in pH2 buffer solution using GCE and gold electrode, as given in Figure4a and 4c respectively. The redox peak current changes were observed during the scan rate study. Faster scan rates cause in narrowing of the diffusion layer, which results in higher current.[53] This is due to the fact that at higher scan rates, the electrode potentials sweep fast enough, resulting in a greater concentration gradient on the electrode surface and causing a higher current.

As illustrated in Figures4a and 4c, an increase in anodic and cathodic peak currents associated with all redox peaks was noticed with an increase in scan rates. The plot of redox peak currents of WO (I/I' and II/II') and the square root of scan rates showed a linear dependence, as illustrated in Figures4b and 4d for GC and gold electrodes respectively. This phenomenon demonstrates that the electrochemical process is diffusion-limited up to a scan rate of $100mVs^{-1}$.

2.2. Electrochemical Behaviour of Multilayer of $NH_4P_5W_{30}$ POM on GC and Gold Electrodes

The $NH_4P_5W_{30}$ POM was immobilised onto the surface of the GCE and gold electrode employing the LBL self-assembly method using PEI as the cationic layer (Section2.3.2.). MBA was used as a preliminary layer for the gold electrode as mentioned in the procedure. The growth of the multilayer films after each layer deposition was monitored using the CV technique in pH2 buffer solution. Figures5a and 5b show the CV response obtained for multilayer film consisting of eight layers of PEI and $NH_4P_5W_{30}$ POM on GCE and gold electrode, which represented as GCE/$(PEI/NH_4P_5W_{30})_8$ and Au/MBA$(PEI/NH_4P_5W_{30})_8$, respectively. The CV pattern observed for the $NH_4P_5W_{30}$ multilayer film is different from what has been seen in the POM's solution behaviour. Five reversible redox couples (I/I', II/II', III/III', IV/IV' and V/V') associated with WO fragments of $NH_4P_5W_{30}$ POM are observed on the GCE. The redox couples represented as WO I/I', II/II', III/III', IV/IV' and V/V' are observed with $E_{1/2}$ values of -0.218, -0.315, -0.389, -0.440 and -0.599V *vs* Ag/AgCl respectively. Likewise, four well-defined redox couples named WO I/I′, II/II′, III/III′ and IV/IV′ prominent for the WO redox processes with $E_{1/2}$ values of -0.221, -0.320, -0.395, and -0.443V *vs* Ag/AgCl were also observed at the gold electrode. What is apparent is that the WO I/I′ and WO-II/II′ redox waves seen in the solution behaviour of $NH_4P_5W_{30}$ POM on both GCE and gold electrode (Figure3) were split into two consecutive bielectronic redox peaks when the POM was immobilised onto the respective electrode surfaces. The splitting of redox

peaks is reasonable due to the strong electrostatic interactions of $NH_4P_5W_{30}$ POM and PEI, which can influence the electron transport mechanism of the redox reactions.[51,54,55] Furthermore, the splitting of peaks also depends on the accessibility of the proton from the electrolyte solution. Therefore, the WO I/I′, II/II′, III/III′ and IV/IV′ redox pairs seen on both the GCE and the gold electrode are bielectronic in nature. The WO V/V' measured for GCE is analogously bielectronic, as the peak difference correlates to the rest of the redox couples.

The electrochemical data of multilayer film on GCE and gold electrodes are summarised in Table2. The cationic PEI layer is not showing any electrochemistry in the $(PEI/NH_4P_5W_{30})_8$ multilayer assembly in pH2 buffer solution (FigureS1). Further characterisation of the $NH_4P_5W_{30}$ POM modified film on the ITO electrode was carried out using FT-IR spectroscopy and given in FigureS2.

Figure6a and 6b shows the series of the CVs obtained during the construction of the multilayer film of $NH_4P_5W_{30}$ POM on GCE and gold electrode respectively in pH2 buffer solution. As can be seen from Figure6, there is progress in the growth of the anodic and cathodic peak current with layer number, which means designating that there is a growth in the adsorption of material in the course of each deposition step onto the electrode surface. The continuous increase in the redox peak currents was prominent for all the WO redox processes with increasing layer numbers. The charge required for a full reduction of the electroactive species is given by the area under the reduction wave which can be represented as (1):[56]

$$Q=nFA\Gamma \quad (1)$$

where Q (C) is the charge passed associated with a particular redox process, Γ ($molcm^{-2}$) is the surface coverage for the surface-confined active species, n is the number of transferred electrons (taken as n=2), A is the area of the electrode in cm^2 and F (96,485 $Cmol^{-1}$) is Faraday's constant.

From equation(2), the average surface coverage values for the surface-confined species can be calculated as:

$$\Gamma = \frac{Q}{nFA} \quad (2)$$

Figure 6b and 6d represents the dependence of calculated surface coverage on the GC and gold electrode respectively, Γ_{ox} and Γ_{red} for WO I/I′ and II/II′ redox process with layer numbers. The increase in surface coverage illustrates the successful grafting of PEI and the $NH_4P_5W_{30}$ POM multilayers on GC and gold electrodes.

2.2.1. Scan Rate Dependence of the Peak Currents

For investigating the relationship between scan rates and WO redox peak currents, cyclic voltammetric measurements were performed on the GCE/$(PEI/NH_4P_5W_{30})_8$ and Au/MBA/$(PEI/NH_4P_5W_{30})_8$ multilayer film in pH2 buffer solution at scan rates from 10 to 100mVs^{-1}. The oxidation and reduction peaks show a corresponding increase in current magnitude with the increase in scan rate as is seen in Figures7a and 7c. As the electron transfer reactions took place rapidly on the modified electrode surface, the potential didn't considerably move with increased scan rate.[57] Moreover, the cathodic to anodic peak current ratios of the WO-II redox pair are close to unity (I_{pc}/I_{pa}): ~1.06 for GCE and ~1.21 for gold electrode. This means that the redox activities of the immobilised POMs in the $(PEI/NH_4P_5W_{30})_8$ multilayer film are fast, surface-confined electron transfer processes unaffected by diffusion.[56,58]

The peak currents, I_p (A) varying with the scan rate, v (Vs^{-1}) observed in the voltammograms can be described using the equation(3):

$$I_p = \frac{n^2 F^2}{4RT} A\Gamma v \quad (3)$$

where R is the ideal gas constant and T (K) is the temperature.[59] The linear dependency of the anodic and cathodic peak currents of WO (I/I' and II/II') with the scan rates are shown in Figures7b and 7d, revealing that the multilayer film is electroactive and well attached to the electrode surface. Also, the WO I/I' and WO-II/II' electrochemical processes are found to be surface-confined up to 100mVs^{-1} scan rate for both the GC and gold electrodes.

On immobilisation, the peak-to-peak separations of the WO redox processes on GC and gold disk electrodes were observed to be smaller when compared with the $NH_4P_5W_{30}$ POM's solution behaviour, as expected for thin layer behaviour. The theoretical ΔE_p value for an ideal reversible surface-confined redox couple is zero. For the WO redox couples, ΔE_p values observed at a lower scan rate are higher than the expected value, stressing that the kinetics of the redox processes are kinetically slow when compared to the experiment time scale.[60,61]

2.2.2. pH Effect

To study the stability of multilayer film at different pHs, the cyclic voltammetric response of $(PEI/NH_4P_5W_{30})_8$ multilayer film which was constructed on both the GCE (FigureS3) and gold electrode (FigureS4) was recorded in buffer solutions with pHs of 2, 3, 4, 5, 6, and 7. As seen in FigureS3a-c, the multilayer film on the GCE exhibited clear redox peaks at all of these pH buffer solutions, indicating that the multilayer film was stable within the given range. Consistently, the CV of multilayer film $MBA/(PEI/NH_4P_5W_{30})_8$ modified on the gold electrode (FigureS4) also showed stable redox peaks at all the pH solutions. When CVs of $(PEI/NH_4P_5W_{30})_8$ were recorded from acidic to alkaline pH, the redox peaks associated with the WO moiety of the multilayer film shifted in the negative potential direction and underwent peak splitting on both the GCE and gold electrode, which is a common feature of POMs.[62] The WO- I/I' peak broadened in pH3 and both the oxidation and reduction peaks split into two monoelectronic peaks in pH4 buffer solution, which were labelled as I_a/I'_a and I_b/I'_b. This phenomenon was observed for the multilayer films on both GC

and gold electrodes (FigureS3b and S4b). The monoelectronic peaks I_a/I_a' and I_b/I_b' becomes more distinctly visible in higher pH buffers (FigureS3c and S4c). The change in the electrochemical behaviour of POM with different pH electrolytes confirms the involvement of proton migration accompanying the redox process. The redox peak currents dropping with an increase in pH was noticed at GC and gold electrodes which indicates that the multilayer film is relatively stable under acidic conditions. This is because the protons in acidic buffers stabilise the POM structure during the redox reaction.[63]

The electrochemical properties of POM in different pH buffer solutions can be explained as follows. The addition of electrons to the POM's pristine form may trigger a pertinent change in the POM's molecular structure by coulombic repulsion, which may eventually affect its structural stability. To neutralise the excess negative charge accumulation on the POM, protons are uptaken by the solvation effect.[64] The consecutive electron transfers of POMs occurred usually via the EEC mechanism, the ECE mechanism, or/and disproportionation reactions. POM protonation is the general chemical step and the possible one, which can be represented as follows:[65]

$$[NH_4P_5W_{30}]^{14-}+mH^{+}+ne^{-} \rightarrow H_m[NH_4P_5W_{30}]^{(14-m+n)-} \quad (4)$$

However, the concentration of protons is significantly reduced with an increase in the pH of the buffer solutions, which influences the electron transfer kinetics and necessitates the application of more negative potential to achieve appreciable current flow. As a consequence, an increase in the values of ΔEp can be seen compared to the anticipated values. Upon going to a higher pH, the ΔEp increases, and the response tends asymptotically toward splitting into two redox waves.[66,67] A similar pattern was reported for Preyssler POM in solution behaviour with varying pH.[34]

FiguresS3d and S4d show the plot of $E_{1/2}$ of the peak WO (III, IV, and V) and WO (II, III, and IV) vs pH for the GCE and gold electrode, respectively. It can be seen from the pH plots in FiguresS3d and S4d that the number of protons involved in the redox processes is the same as the electron numbers as taken from the slope values of between 49 and 62mV per decade change in pH.

$$\frac{dE}{dpH} = -59.1\frac{m}{n}(mVpH^{-1}) \quad (5)$$

where m is the number of protons and n is the number of electrons involved in the redox process.[68]

2.2.3. Stability

The GCE/(PEI/$NH_4P_5W_{30}$)$_8$ and Au/MBA/(PEI/$NH_4P_5W_{30}$)$_8$ multilayer was cycled 100 times in a pH2 buffer solution between their redox states at the scan rate of 10mVs^{-1} for investigating its endurance performance. FiguresS5a and S5b show the CV responses of the first and 100th cycles obtained for the GCE/(PEI/$NH_4P_5W_{30}$)$_8$ and Au/MBA/(PEI/$NH_4P_5W_{30}$)$_8$ multilayer film, respectively. From the figures, it was noticed that the multilayer film on both electrodes retained remarkably the same redox peak currents after the continuous redox switching test, which attributes to the significant stability of the film without leaching out into the electrolyte solution. The surface coverage at the 1st and 100th potential cycle was calculated for both the multilayer films GCE/(PEI/$NH_4P_5W_{30}$)$_8$ and Au/MBA/(PEI/$NH_4P_5W_{30}$)$_8$ (using equation2) from the cathodic and anodic charges of WO-I/I′ and WO- II/II′ as given in table S2 and S3, respectively.

2.2.4. Electrochemical Impedance Spectroscopy

AC impedance spectroscopy is an established electrochemical characterisation technique which elucidates the electrode-electrolyte interface by measuring a disturbing signal in response to a small amplitude sinusoidal potential or current.[69] This technique

provides a quantitative determination of both kinetic and diffusion parameters for a solution as well as phase redox-active systems. Electrochemical impedance spectra were recorded after the deposition of each PEI and $NH_4P_5W_{30}$ POM layer for estimating the deviation in electrical properties with film structure and thickness. The monoelectronic potassium ferricyanide/ferrocyanide ($[Fe\ (CN)_6]^{3-/4-}$) couple has been used as the redox probe to monitor the electrical parameters of ($PEI/NH_4P_5W_{30}$) multilayer film through the employment of impedance spectroscopy with open circuit potential as the applied potential. The obtained Nyquist plots during various stages of film formation on the GCE and gold electrode were depicted in Figures8<figr8>a and 8b. In the Nyquist plots, the imaginary component of impedance ($-Z''$) is plotted over the real component (Z') as a function of frequency.

The Nyquist plots consist of a semicircle at a higher frequency region related to the interfacial electron transfer kinetics as well as an inclined line region corresponding to the diffusion-controlled region at a lower frequency. The Nyquist plot simulations were carried out based on the Randles circuit (Insert in Figures8<xfigr8>a and 8b), which is a well-established model for interpreting the characteristics of a multilayer system when in contact with an electrolyte interface.[70] The circuit consists of double-layer capacitance (C_{dl}), charge transfer resistance (R_{ct}), Warburg impedance (Z_W) and solution resistance (R_S). In the circuit, R_S is in series with C_{dl} while C_{dl} is parallel with Z_W and R_{ct}, which is together known as a diffusional branch. Because of the nonideal interfacial features of the electrode surface, C_{dl} is replaced with a constant phase element (CPE).[8] Given by, $CPE=-1/(Ci\omega)n$, where C is the capacitance, which describes the charge separation at the double layer interface, ω is the frequency in rad s^{-1} and the n exponent is due to the heterogeneity of the surface. The CPE is closely related to the porosity and roughness of electrodes.[70,71] The numerical values for R_S, R_{ct}, CPE and Z_W were extracted using the Randles equivalent circuit and summarised in TablesS4 and S5 for the GCE and gold electrode, respectively.

The solution resistance for both the gold and GC electrodes remained similar after each PEI and POM deposition. The resulting change of the R_{ct} values during the layer deposition is plotted over the number of layers in FigureS6a and S6b for the GC and gold electrodes, respectively. To understand these results it is necessary to emphasise that the PEI and POM deposition can cause an increase in film thickness which may change the overall film porosity by filling in existing pores or opening up new pores. If the porosity diminishes with layer thickness, the permeation of ($[Fe(CN)_6]^{3-/4-}$) redox couple becomes difficult and the electrical impedance increases proportionally with the film construction. Furthermore, from FiguresS6a and S6b, it is noted that the R_{ct} values are elevating concerning the number of layers deposited. This can be explained as follows: for the initial layers, the redox process is dominated by diffusion control, but with increased layer depositions, the redox process becomes kinetically controlled with higher R_{ct} values. However, the R_{ct} values are showing an enormous increase for the POM outer layers when compared to the PEI outer layers. This applies to the relationship between the overall outer layer charge and the anionic ($[Fe(CN)_6]^{3-/4-}$) redox couple. When the outer layer is anionic POM, electrostatic repulsion is experienced with the anionic redox probe, resulting in increased resistance, whilst the outer cationic PEI layer yields less resistance. Moreover, as the film grows, it becomes less porous. Non-uniformities on the surface play a significantly larger role when the charges of the electroactive species and the outermost layer are opposite, resulting in a stronger influence of surface roughness on species transport.[70,71] This can be perceived as with each monolayer deposition the vicinity of the redox probe to the underlying electrode surface diminishes due to the reduced number of pathways as well as increased pathway length. This can be viewed as an escalating of R_{ct} values with layer number, which exhibited a non-linear relationship from the 1st, 2nd, and 3rd bilayers to the 4th bilayer, which is probably attributed to the changes in film texture within the inner and outer layers.[72] The gold electrode has much higher R_{ct} values for the 4th bilayer than the GC electrode, which could be attributed to the initial MBA

layer. Finally, the values of the CPE are much lower for both electrodes are lower and significantly different, giving indications that the multilayer also has a different internal structure on different electrode surfaces.

For checking the reliability of the impedance spectra, cyclic voltammetric responses for the ($[Fe(CN)_6]^{3-/4-}$) redox couple were recorded with varying stages of film deposition. FigureS7a displayed a well-defined redox peak associated with Fe^{2+}/Fe^{3+} in 0.1M KCl solution at the ($PEI/NH_4P_5W_{30}$) modified GCE until the 4^{th} bilayer. Similar to the GCE response, the ($MBA/PEI/NH_4P_5W_{30}$) modified gold electrode showed clear redox peaks corresponding to the ($[Fe(CN)_6]^{3-/4-}$) redox probe until the 4^{th} bilayer (FigureS7b). Whereas further deposition of PEI and POM on GCE, caused the shrinking of both anodic and cathodic peak currents with an increase in separation of peak potentials as represented in FigureS7a and S7b, indicating that the Fe^{2+}/Fe^{3+} redox process shifted from reversible to quasi-reversible system. These changes in peak currents and peak potentials are consistent with the electrochemical impedance results. With the layer growth on GCE and gold electrode, the film porosity lessens which makes the diffusion of the redox probe through the multilayer film challenging. Moreover, when the outer layer is anionic POM, the proximity of the anionic redox probe to the electrode surface becomes more difficult due to electrostatic repulsive force. Thus the overall outer layer charge can control the mobility of the anionic redox probe. This concludes that the deviations of cyclic voltammetric responses were sensitive not only to film thickness but also to the overall charge of the outer layer.

2.3. Electrochemical Quartz Crystal Measurement

It is known that EQCM is a sophisticated electrochemical tool for monitoring film growth and film dissolution during potential sweeping. In this study, EQCM is employed for monitoring the deposition of $NH_4P_5W_{30}$ POM during the LBL technique on a gold quartz electrode by recording the frequency variation with time. Figure9<figr9>a demonstrates the

change of frequency as a function of time during POM deposition steps. As seen in the figure, a frequency decrease was observed with the adsorption of each POM layer, which was associated with an increase in POM concentration on the electrode surface. According to the Sauerbrey equation(6), the changes in the resonance frequency of the quartz crystal electrode are proportional to the mass accumulated on the crystal assuming a rigid film is formed. The relationship between the frequency shift and the mass adsorbed on the quartz crystal electrode is given as follows.[73]

$$\Delta f = -\frac{2f_0^2}{A\sqrt{\rho_q \mu_q}}\Delta m \quad (6)$$

where Δf is the change in resonance frequency, f_0 (7.995MHz) is the fundamental resonance frequency, Δm is the change in electrode mass, A (0.196cm^2) is the surface area of the electrode, μ_q (2.947×10^{11}gcm^{-1}s^{-1}) is the shear modulus of quartz, ρ_q (2.648gcm^{-3}) is the density of quartz.

A frequency decrease of 26.80Hz was observed during the first POM layer deposition, which corresponds to a POM mass deposition of 35.91ngcm^{-2}. The adsorption of the second and third POM layers causes a frequency decrease of 43.17Hz and 59.85Hz which corresponds to a mass increase of 57.85ngcm^{-2} and 80.20ngcm^{-2} respectively. The frequency does not appear to be decreasing upon the deposition of the fourth POM layer and the other successive layers with layer deposition. In this context, the multilayer film cannot be considered rigid, and the Sauerbrey equation is no longer applicable for calculating the mass change of the successive layers.

After each POM deposition step, the cyclic voltammetric responses were recorded in a pH2 buffer for monitoring the growth of the film on the gold quartz crystal electrode as given in Figure9b. What is evident from the figure is that the multilayer film formation is happening in a non-uniform pattern due to some weekly-bound POM molecules that stick to the electrode surface even after the cleaning step. Figures9c and d illustrate the cyclic

voltammogram of Au/MBA/(PEI/$NH_4P_5W_{30}$)$_8$ film and corresponding EQCM responses respectively, recorded in pH2 buffer solution at a scan rate of 50mVs^{-1} for 10 cycles. For making the multilayer film fully electroactive and attaining a steady-state voltammogram, it might be required to cycle several times and this phenomenon is termed as a break-in effect.[74] As a result of the break-in effect, the initial four cycles had a significantly different behaviour than other cycles. This difference included the variation in peak current as well as the resonance frequency of the modified quartz crystal electrode. These observations comprehend the removal of loosely bound $NH_4P_5W_{30}$ POM ions from the multilayer film. The combination of EQCM and CV attribute information about the nature of the ions participating in the sorption process for compensating overall film charge.

Typically, during the reduction sweep, electrons are given to the film from the electrode; as a result, cation insertion from the electrolyte solutions takes place to balance the film‘s excess negative charge. The electrons are transported from the multilayer film to the electrode when the potential changes to positive, while SO_4^{2-} ions from the electrolyte are adsorbed into the film to counteract the positive charge of the film. However, as previously mentioned, during the earliest cycles, the loosely attached POM molecules are leaching out from the surface. Despite the addition of SO_4^{2-} ions, this is the cause of the rise in frequency during both oxidation and reduction. After the initial cycles, the multilayer film becomes stable, with neither restructuring nor changes in redox behaviour. For our system, the change in frequency caused by the movement of cation and anion during oxidation and reduction was difficult to observe. The successive cyclic voltammograms overlay each other, and the change in frequency and potential is also consistent with voltammetric results.[75--77]

3. Conclusions

The solution electrochemistry of the Preyssler type $(NH_4)_{14}[NaP_5W_{30}O_{110}].44H_2O$ ($NH_4P_5W_{30}$) POM in pH2 buffer solution was studied with GCE and gold electrode.

$NH_4P_5W_{30}$ POM was successfully immobilised onto the surface of the glassy carbon electrode, gold electrode and gold quartz electrode using the layer-by-layer self-assembly method. The formation of stable and reproducible multilayer assemblies consisting of a cationic polyethyleneimine layer and anionic $NH_4P_5W_{30}$ POM completely relies on electrostatic attractions and Van der Waals forces. The film's construction was monitored and characterised employing cyclic voltammetry, AC impedance spectroscopy and electrochemical quartz crystal microbalance (EQCM) techniques. It has been shown that the combination of EQCM monitoring of the LBL film deposition, EIS and CV, can give valuable information about the multilayer deposition. Five and four reversible redox couples associated with tungsten-oxo (WO) frameworks were observed for $NH_4P_5W_{30}$ POM multilayer film on GCE and gold electrodes, respectively. Scan rate studies of the multilayer film showed that the WO peak currents were proportional to scan rate up to $100mVs^{-1}$ indicating the thin layer behaviour of the film. The film showed pH-dependent redox activity associated with the WO framework with a negative potential shift with an increase in pH. The stability of the multilayer film was analysed by conducting a continuous redox switching test and it seemed remarkably stable with less leaching of $NH_4P_5W_{30}$ POM ions into the electrolyte. AC impedance studies of the multilayer film using a monoelectronic ($[Fe(CN)_6]^{3-/4-}$) redox probe yielded charge transfer resistances, R_{ct}, values. The R_{ct} values seemed to rise with an increase in layer number and are dependent upon the nature of the film's outer layer. An in-situ EQCM was used to illustrate the redox-induced migration of ions into POM-based multilayer films. The measurements were used to monitor film dissolution during the break-in process. During the initial cyclic voltammograms, a frequency increase was noticed, indicating the leaching out of POM ions from the film during the reduction segment and doping of both POM ions and electrolyte anion during the oxidation segment. This work has demonstrated that the combination of POM and the layer-by-layer approach is ideal for creating a hybrid film of

stable electrocatalysts with a nanolayer thickness that can be used for a variety of applications such as water splitting, biosensors, energy storage devices, and so on.

Acknowledgements

This work was supported by the Higher Education Authority in Ireland. The authors acknowledge Dundalk Institute of Technology for instrumental support in performing the electrochemical experiments and IPCM, Sorbonne University, for POM synthesis support.

Conflict of Interests

The authors declare no conflict of interest.

Data Availability Statement

The data that support the findings of this study are available from the corresponding author upon reasonable request.

<lit1> M. Ammam, *J. Mater. Chem. A* **2013**, *1*, 6291--6312</jnl>.

<lit2> X. Chen, Y. Zhou, V.A.L. Roy, S.T. Han, *Adv. Mater.* **2017**, *30*, 1--9</jnl>.

<lit3> H. Khalilpour, P. Shafiee, A. Darbandi, M. Yusuf, S. Mahmoudi, Z. MoazzamiGoudarzi, S. Mirzamohammadi, *J Compos Compd* **2021**, *3*, 129--139</jnl>.

<lit4> I. Sakthinathan, J. Köhling, V. Wagner, T. McCormac, *ACS Appl. Mater. Interfaces* **2023**, *15*, 2861--2872</jnl>.

<lit5> D. Qi, H. Chu, K. Wang, X. Li, J. Huang, *ChemistrySelect* **2018**, *3*, 12469--12477</jnl>.

<lit6> X. Chen, J. Pan, J. Fu, X. Zhu, C. Zhang, L. Zhou, Y. Wang, Z. Lv, Y. Zhou, S.T. Han, *Adv. Electron. Mater.* **2018**, *1800444*, 1--9</jnl>.

<lit7> J. Li, W. Chen, L. Chen, X. Zheng, G. Zhu, E. Wang, *Adv. Opt. Mater.* **2018**, *6*, 1--12</jnl>.

<lit8> A. Yaqub, S.R. Gilani, S. Bilal, A. Hayat, A. Asif, S.A. Siddique, *ACS Omega* **2022**, *7*, 149--159</jnl>.

<lit9> J.M. Clemente-Juan, E. Coronado, A. Gaita-Ariñoa, *Chem. Soc. Rev.* **2012**, *41*, 7464--7478</jnl>.

<lit10> J. Wang, Z. Tao, T. Tian, J. Qiu, H. Qian, Z. Zha, Z. Miao, Y. Ma, H. Wang, *Chem. Eng. J.* **2021**, *416*, 1--10</jnl>.

<lit11> S. Hartung, N. Bucher, H.Y. Chen, R. Al-Oweini, S. Sreejith, P. Borah, Z. Yanli, U. Kortz, U. Stimming, H.E. Hoster, M. Srinivasan, *J. Power Sources* **2015**, *288*, 270--277</jnl>.

<lit12> S. Barman, S.S. Sreejith, S. Garai, R. Pochamoni, S. Roy, *ChemPhotoChem* **2019**, *3*, 93--100</jnl>.

<lit13> L.C. Palilis, M. Vasilopoulou, A.M. Douvas, D.G. Georgiadou, S. Kennou, N.A. Stathopoulos, V. Constantoudis, P. Argitis, *Sol. Energy Mater. Sol. Cells* **2013**, *114*, 205--213</jnl>.

<lit14> Z.X. Yang, P. Huang, L. Zhao, M. Zhang, Y.T. Zhang, Z.M. Su, *Inorg. Chem. Commun.* **2014**, *44*, 195--197</jnl>.

<lit15> P. Huang, X.G. Han, X.L. Li, C. Qin, X.L. Wang, Z.M. Su, *CrystEngComm* **2016**, *18*, 8722--8725</jnl>.

<lit16> M. Petruleviciene, K. Turuta, I. Savickaja, J. Juodkazyte, A. Ramanavicius, *J. Electroanal. Chem.* **2023**, *951*, 1--10</jnl>.

<lit17> M. Petruleviciene, J. Juodkazyte, M. Parvin, A. Tereshchenko, S. Ramanavicius, R. Karpicz, U. Samukaite-Bubniene, A. Ramanavicius, *Materials (Basel)* **2020**, *13*, 1--14</jnl>.

<lit18> M. Petruleviciene, I. Savickaja, J. Juodkazyte, A. Ramanavicius, *Chemosensors* **2023**, *11*, 1--14</jnl>.

<lit19> P.A. Shinde, S.C. Jun, *ChemSusChem* **2020**, *13*, 11--38</jnl>.

<lit20> L. Ni, J. Gu, X. Jiang, H. Xu, Z. Wu, Y. Wu, Y. Liu, J. Xie, Y. Wei, G. Diao, *Angew. Chem. Int. Ed.* **2023**, *62*, 1--9</jnl>.

<lit21> Z. Zeb, Y. Huang, L. Chen, W. Zhou, M. Liao, Y. Jiang, H. Li, L. Wang, L. Wang, H. Wang, T. Wei, D. Zang, Z. Fan, Y. Wei, *Coord. Chem. Rev.* **2023**, *482*, 1--53</jnl>.

<lit22> C. Gu, Z. Wang, Y. Pan, S. Zhu, Z. Gu, *Adv. Mater.* **2023**, *35*, 1--26</jnl>.

<lit23> J.A. Fernández, X. Lopez, C. Bo, C. deGraaf, E.J. Baerends, J.M. Poblet, *J. Am. Chem. Soc.* **2007**, *129*, 12244--12253</jnl>.

<lit24> F.F. Bamoharram, M.M. Heravi, P. Ardalan, T. Ardalan, *React. Kinet. Mech. Catal.* **2010**, *100*, 71--78</jnl>.

<lit25> C. Qin, X.Z. Song, S.Q. Su, S. Dang, J. Feng, S.Y. Song, Z.M. Hao, H.J. Zhang, *Dalton Trans.* **2012**, *41*, 2399--2407</jnl>.

<lit26> X. Wang, J. Li, A. Tian, H. Lin, G. Liu, H. Hu, *Inorg. Chem. Commun.* **2011**, *14*, 103--106</jnl>.

<lit27> T.P. Hu, Y.Q. Zhao, Z. Jagličić, K. Yu, X.P. Wang, D. Sun, *Inorg. Chem.* **2015**, *54*, 7415--7423</jnl>.

<lit28> H.M. Zhao, H.M. Gan, L. Zhao, Z.M. Su, *Inorg. Chem. Commun.* **2020**, *113*, 1--5</jnl>.

<lit29> M.J. Turo, L. Chen, C.E. Moore, A.M. Schimpf, *J. Am. Chem. Soc.* **2019**, *141*, 4553--4557</jnl>.

<lit30> J. Shi, Y. Xiong, M.J. Zhou, L. Chen, Y. Xu, *RSC Adv.* **2017**, *7*, 55427--55433</jnl>.

<lit31> H.T. Zhu, W.S. Tang, Y.Y. Ma, Y.H. Wang, H.Q. Tan, Y.G. Li, *CrystEngComm* **2021**, *23*, 2071--2080</jnl>.

<lit32> A. Hayashi, H. Ota, X. López, N. Hiyoshi, N. Tsunoji, T. Sano, M. Sadakane, *Inorg. Chem.* **2016**, *55*, 11583--11592</jnl>.

<lit33> M.M. Heravi, F.F. Bamoharram, G. Rajabzadeh, N. Seifi, M. Khatami, *J. Mol. Catal. A* **2006**, *259*, 213--217</jnl>.

<lit34> M.H. Alizadeh, S.P. Harmalker, Y. Jeannin, J. Martin-Frer, M.T. Pope, *J. Am. Chem. Soc.* **1985**, *107*, 2662--2669</jnl>.

<lit35> S. Liu, D.G. Kurth, H. Möhwald, D. Volkmer, *Adv. Mater.* **2002**, *14*, 225--228</jnl>.

<lit36> S. Saneinezhad, F.F. Bamoharram, A.M. Mozhdehi, A.H. Sharifi, A. Ayati, M. Pordel, J. Baharara, M. Sillanpää, *Arab. J. Chem.* **2020**, *13*, 4644--4660</jnl>.

<lit37> D.C. Huez, S. Renaudineau, F.Volatron, A. Proust, Vuillaume, *Nanoscale* **2023**, 10634--10641</jnl>.

<lit38> I. Creaser, M.C. Heckel, R.J. Neitz, M.T. Pope, *Inorg. Chem.* **1993**, *32*, 1573--1578</jnl>.

<lit39> D.M. Fernandes, H.M. Carapuça, C.M.A. Brett, A.M.V. Cavaleiro, *Thin Solid Films* **2010**, *518*, 5881--5888</jnl>.

<lit40> G.R. Xu, S.H. Wang, H.L. Zhao, S.B. Wu, J.M. Xu, L. Li, X.Y. Liu, *J. Membr. Sci.* **2015**, *493*, 428--443</jnl>.

<lit41> M. Genovese, Y.W. Foong, K. Lian, *J. Electrochem. Soc.* **2015**, *162*, A5041--A5046</jnl>.

<lit42> G. Bajwa, M. Genovese, K. Lian, *ECS J. Solid State Sci. Technol.* **2013**, *2*, M3046--M3050</jnl>.

<lit43> D. Zang, Z. Huo, S. Yang, Q. Li, G. Dai, M. Zeng, L. Ruhlmann, Y. Wei, *Mater. Today Commun.* **2022**, *31*, 1--11</jnl>.

<lit44> A. vanderStraeten, D. Lefèvre, S. Demoustier-Champagne, C. Dupont-Gillain, *Adv. Colloid Interface Sci.* **2020**, *280*, 1--18</jnl>.

<lit45> B. Ali, T. McCormac, C. Maccato, D. Barreca, G. Carraro, *J. Electroanal. Chem.* **2020**, *858*, 113770</jnl>.

<lit46> K. Ariga, Q. Ji, J.P. Hill, *Adv. Polym. Sci.* **2010**, *229*, 51--87</jnl>.

<lit47> T. Lee, S.H. Min, M. Gu, Y.K. Jung, W. Lee, J.U. Lee, D.G. Seong, B.S. Kim, *Chem. Mater.* **2015**, *27*, 3785--3796</jnl>.

<lit48> M. Genovese, K. Lian, *ACS Appl. Mater. Interfaces* **2016**, *8*, 19100--19109</jnl>.

<lit49> L. Zheng, X. Yao, J. Li, *Curr. Anal. Chem.* **2006**, *2*, 279--296</jnl>.

<lit50> S. Liu, D.G. Kurth, B. Bredenkötter, D. Volkmer, *J. Am. Chem. Soc.* **2002**, *124*, 12279--12287</jnl>.

<lit51> M. Jiang, D. Zhu, J. Cai, H. Zhang, X. Zhao, *J. Phys. Chem. C* **2014**, *118*, 14371--14378</jnl>.

<lit52> M.T.P. Jeannin, Y.J. Martin- Frere, DanielJ. Choi, *Inorg. Synth.* **1990**, *27*, 115--118</jnl>.

<lit53> N. Elgrishi, K.J. Rountree, B.D. McCarthy, E.S. Rountree, T.T. Eisenhart, J.L. Dempsey, *J. Chem. Educ.* **2018**, *95*, 197--206</jnl>.

<lit54> L. Cheng, J.A. Cox, *Electrochem. Commun.* **2001**, *3*, 285--289</jnl>.

<lit55> M. Huang, L. Bi, Y. Shen, B. Liu, S. Dong, *J. Phys. Chem. B* **2004**, *108*, 9780--9786</jnl>.

<lit56> L.R. Bard, A.J.Faulkner, *Fundamentals and Applications. Electrochemical Methods* **2001**</jnl>.<?><?>Dear Author, is this the correct abbreviation of the Journal Title<?><?>

<lit57> S.P. Muthusamy, I. Sakthinathan, N. Yamasaki, T. Ueda, T. McCormac, *Int. J. Electrochem. Sci.* **2024**, *19*, 1--7</jnl>.

<lit58> M. Ammam, B. Keita, L. Nadjo, I.M. Mbomekalle, J. Fransaer, *Electrochim. Acta* **2010**, *55*, 3213--3222</jnl>.

<lit59><book>F. Scholz, *Electroanalytical Methods*, Springer, **2010**</book>.

<lit60> M. Yaqub, J.J. Walsh, T.E. Keyes, A. Proust, C. Rinfray, G. Izzet, T. McCormac, R.J. Forster, *Langmuir* **2014**, *30*, 4509--4516</jnl>.

<lit61> S. Imar, M. Yaqub, C. Maccato, C. Dickinson, F. Laffir, M. Vagin, T. McCormac, *Electrochim. Acta* **2015**, *184*, 323--330</jnl>.

<lit62> X. Wang, Z. Kang, E. Wang, C. Hu, *J. Electroanal. Chem.* **2002**, *523*, 142--149</jnl>.

<lit63> M. Zhou, L. pingGuo, F. yunLin, H. xiaLiu, *Anal. Chim. Acta* **2007**, *587*, 124--131</jnl>.

<lit64><book>J.-M. Savéant, *Elements of Molecular and Biomolecular Electrochemistry: An Electrochemical Approach to Electron Transfer Chemistry*, A JOHN WILEY & SONS, INC., PUBLICATION, **20006**</book>.

<lit65> K. Wearen, S. Imar, B. Ali, T. McCormac, *J. Electroanal. Chem.* **2019**, *832*, 493--499</jnl>.

<lit66> M. Ammam, B. Keita, L. Nadjo, J. Fransaer, *Talanta* **2010**, *80*, 2132--2140</jnl>.

<lit67> S. PitchaiMuthusamy, I. Sakthinathan, T. McCormac, *J. Electroanal. Chem.* **2024**, *952*, 1--10</jnl>.

<lit68> T.M. BushraAli, Indherjith Sakthinathan, Davide Barreca, Chiara Maccato, Joydeb Goura, Ulrich Kortz, *Thin Solid Films* **2023**, *766*, 1--8</jnl>.

<lit69> Q.Z. Luo, Q. Huang, Z. Chen, L. Yao, P. Fu, Z.D. Lin, *Mater. Res. Express* **2018**, *5*, 1--10</jnl>.

<lit70> D.M. Fernandes, M.E. Ghica, A.M.V. Cavaleiro, C.M.A. Brett, *Electrochim. Acta* **2011**, *56*, 7940--7945</jnl>.

<lit71> Q. Ruan, Y. Zhu, F. Li, J. Xiao, Y. Zeng, F. Xu, *J. Colloid Interface Sci.* **2009**, *333*, 725--733</jnl>.

<lit72> N. Anwar, T. McCormac, J.D. Compain, P. Mialane, A. Dolbecq, F. Laffir, *Electrochim. Acta* **2012**, *59*, 1--7</jnl>.

<lit73> J. Kugai, S. Tanaka, S. Seino, T. Nakagawa, T.A. Yamamoto, H. Yamada, *J. Electroanal. Chem.* **2021**, *897*, 1--9</jnl>.

<lit74> J. Bácskai, G. Inzelt, *J. Electroanal. Chem.* **1991**, *310*, 379--389</jnl>.

<lit75> B.D. McCarthy, A.M. Beiler, B.A. Johnson, T. Liseev, A.T. Castner, S. Ott, *Coord. Chem. Rev.* **2020**, *406*, 213137</jnl>.

<lit76> Y. Tang, X. Zeng, *J. Electrochem. Soc.* **2008**, *155*, F82--F90</jnl>.

<lit77> M. Baibarac, I. Baltog, S. Frunza, A. Magrez, D. Schur, S.Y. Zaginaichenko, *Diam Relat Mater* **2013**, *32*, 72--82</jnl>.<?><?>Dear Author, is this the correct abbreviation of the Journal Title<?><?>

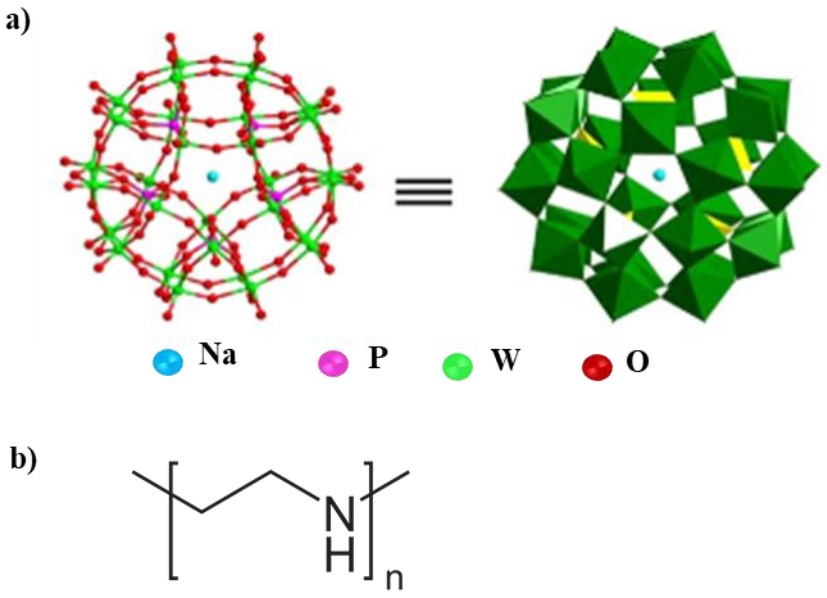

Figure1 (a) The ball-and-stick and polyhedral representation of the Preyssler anion $[NaP_5W_{30}O_{110}]^{14-}$, adapted from[26] (b) Structure of the polyethyleneimine (PEI).

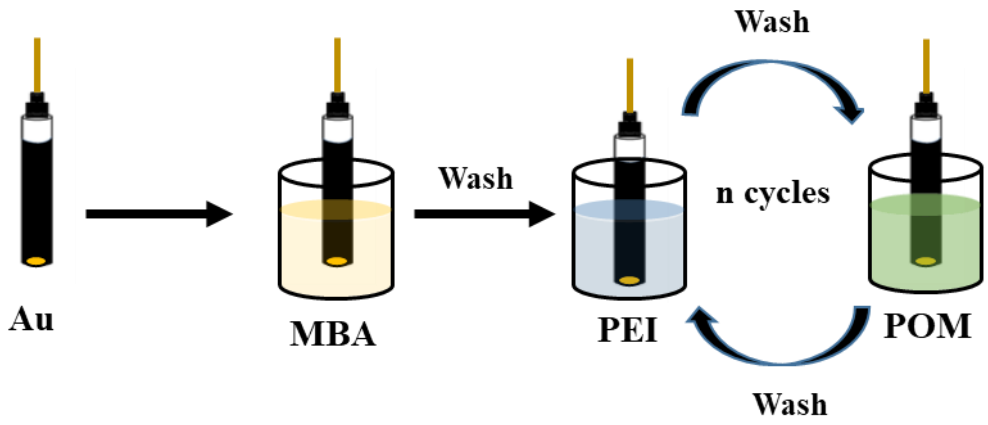

Figure2 A schematic representation of the LBL method for immobilising $NH_4P_5W_{30}$ POM on a gold electrode. The gold electrode was initially functionalised with the negatively charged thiol MBA before being dipped into solutions of positively charged PEI and negatively charged $NH_4P_5W_{30}$ POM.

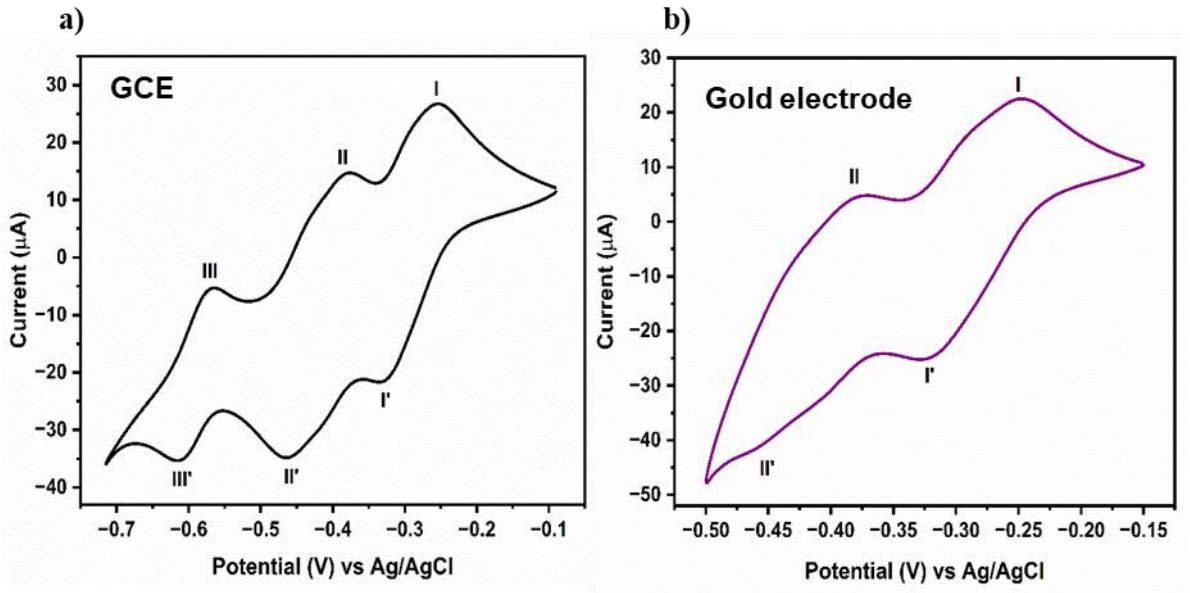

Figure3 Cyclic voltammogram of (a) 2mM $NH_4P_5W_{30}$ POM on GCE and (b) 5mM $NH_4P_5W_{30}$ POM on gold electrode *vs* Ag/AgCl in pH2 buffer at a scan rate of $10mVs^{-1}$.

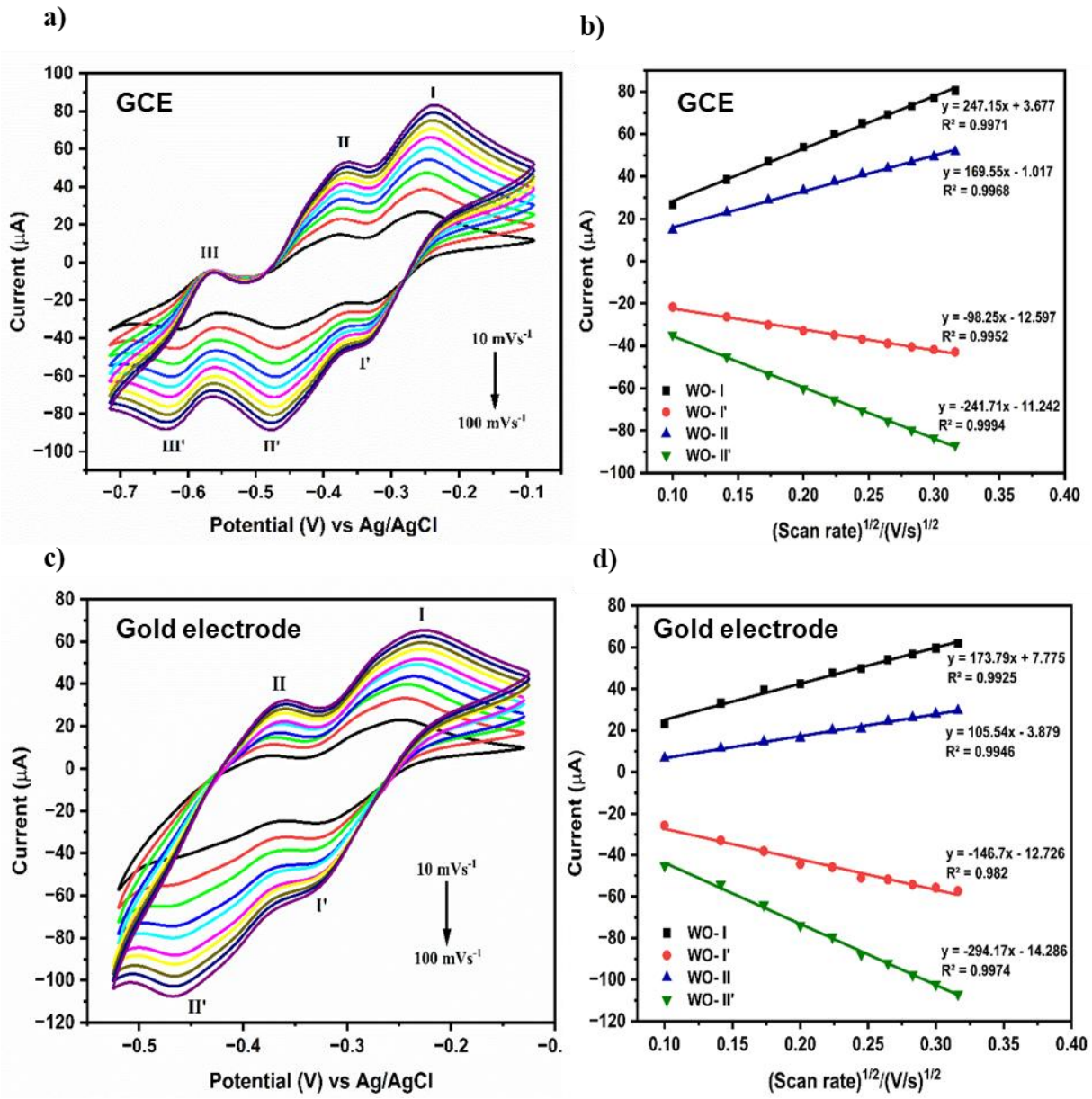

Figure4 Cyclic voltammograms of (a) 2mM $NH_4P_5W_{30}$ POM on GCE and (b) 5mM $NH_4P_5W_{30}$ POM on gold electrode *vs* Ag/AgCl in pH2 buffer solution at a scan rate between 10 and 100mVs^{-1} (from inner to outer curve). (b) and (d) The plot of WO<C->I/I′ and WO-II/II′ peak currents *vs* square root of scan rate, data taken from Figure4<xfigr4>a and 4c respectively.

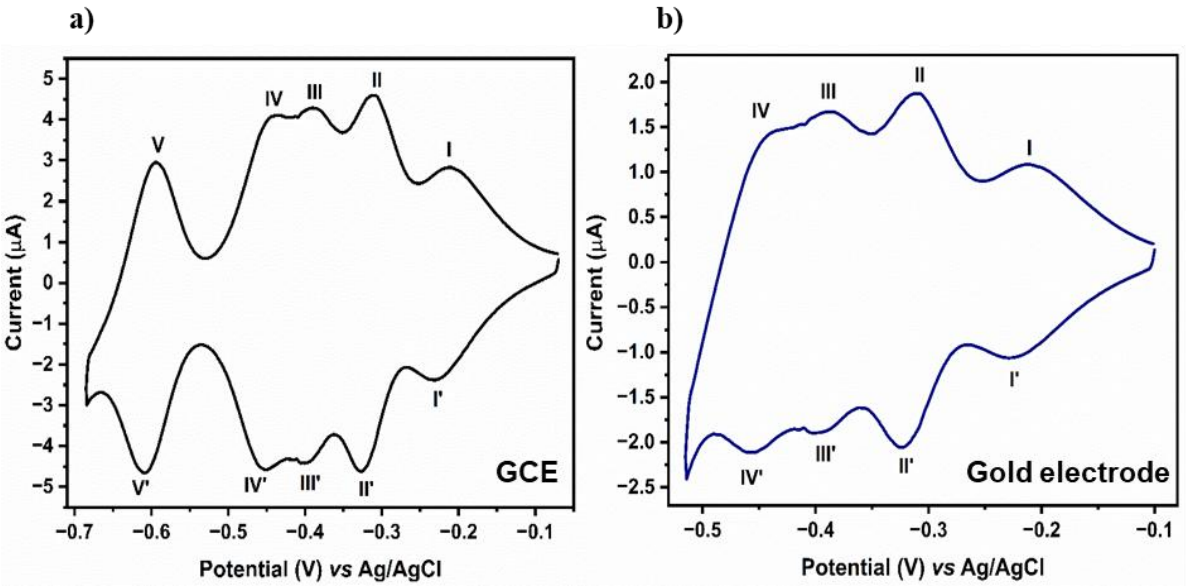

Figure5 Cyclic voltammogram of (a) GCE/$(PEI/NH_4P_5W_{30})_8$ and (b) Au/MBA/$(PEI/NH_4P_5W_{30})_8$ *vs* Ag/AgCl in pH2 buffer solution at a scan rate 10mVs^{-1}.

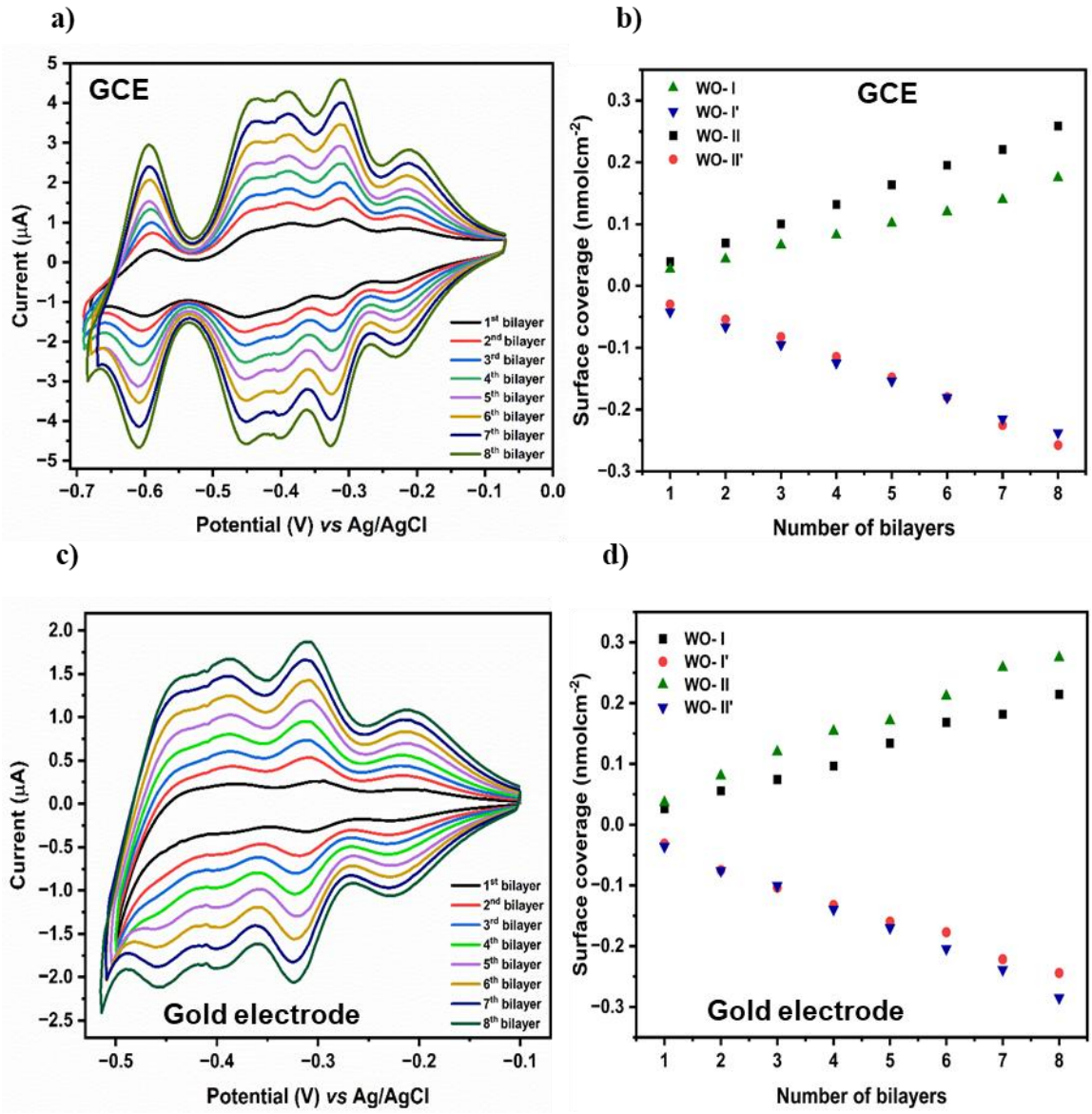

Figure6 (a) Cyclic voltammograms of (a) GCE/$(PEI/NH_4P_5W_{30})_{1-8}$ and (c) Au/MBA/$(PEI/NH_4P_5W_{30})_{1-8}$ *vs* Ag/AgCl in pH2 buffer solution at scan rate $10mVs^{-1}$. (b) and (d) The linear plot of surface coverage corresponding to WO- I/I′ and II/II′ *vs* the number of bilayers, data are taken from Figures6<xfigr6>a and 6c, respectively.

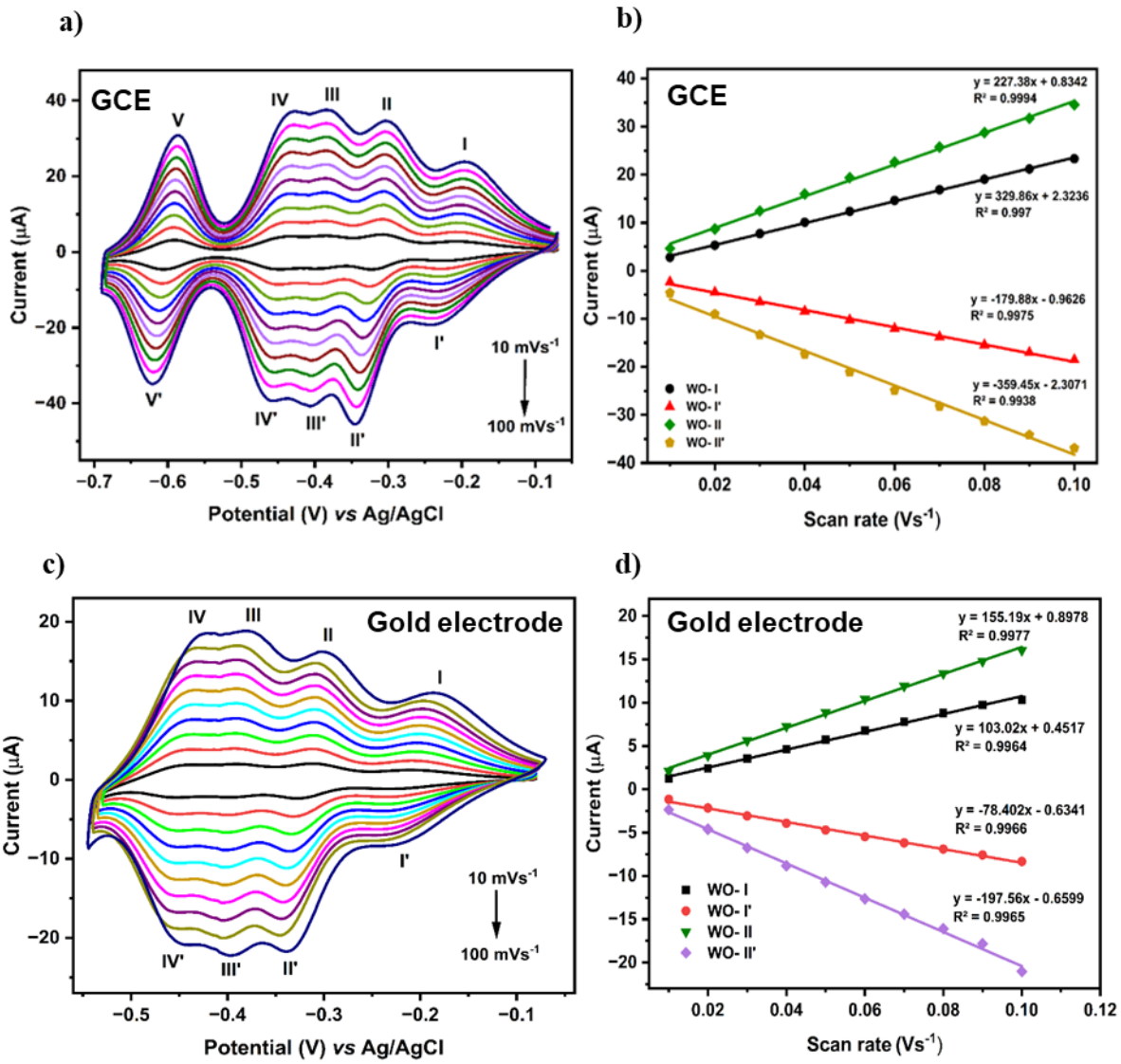

Figure7 Cyclic voltammograms of (a) GCE/$(PEI/NH_4P_5W_{30})_8$ and (b) Au/MBA/$(PEI/NH_4P_5W_{30})_8$ *vs* Ag/AgCl in pH2 buffer at scan rate between 10 and 100mVs^{-1} (from inner to outer curve). (b) and (d) The plot of WO I/I′ and WO II/II′ peak currents *vs* scan rate for the multilayer film data taken from Figure7<xfigr7>a and 7c, respectively.

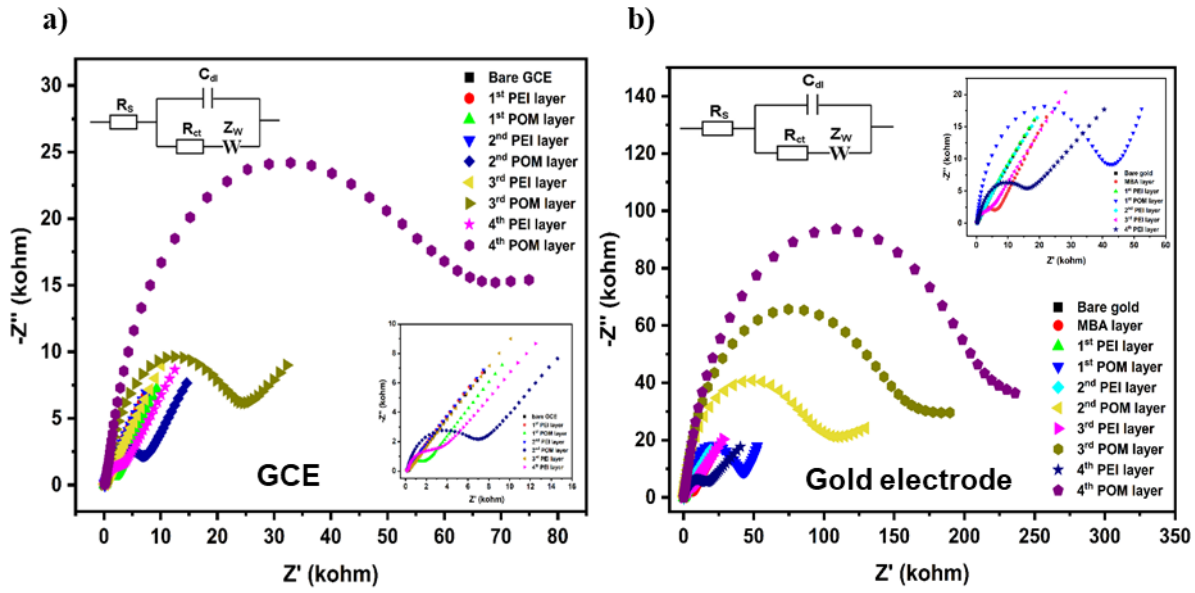

Figure8 (a) Nyquist plots of bare GCE and multilayer film of (PEI/$NH_4P_5W_{30}$) layers on GCE. (b) Nyquist plots of the bare gold electrode and multilayer film of (MBA/PEI/$NH_4P_5W_{30}$) layers on a gold electrode. The frequency range is between 0.01 to 10^6Hz and voltage amplitude was 5mV in each case. The open circuit potential was taken as the applied potential *vs* Ag/AgCl in the presence of 1mM potassium ferricyanide and potassium ferrocyanide (1:1) in 0.1M potassium chloride as a redox probe. Randle's equivalent circuit was used to fit the impedance data that was given in the figures.

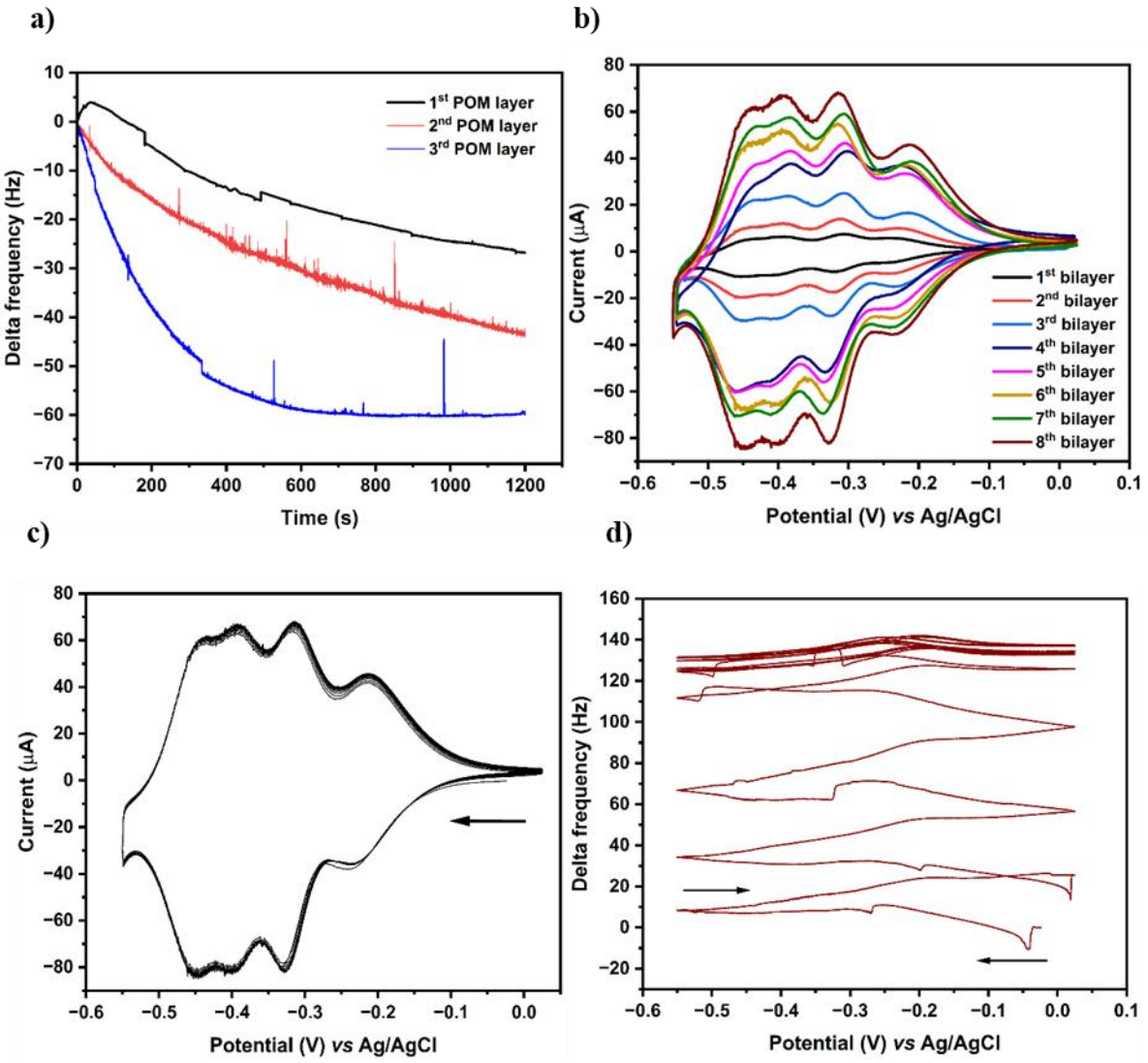

Figure9 (a) The plot of delta frequency *vs* time was recorded during the POM deposition step. (b) Cyclic voltammetric overlay of Au/MBA/$(PEI/NH_4P_5W_{30})_{1-8}$ *vs* Ag/AgCl in pH2 buffer solution at a scan rate of 50mVs^{-1}. (c) Cyclic voltammetric break-in of Au/MBA/$(PEI/NH_4P_5W_{30})_8$ *vs* Ag/AgCl in pH2 buffer solution at a scan rate of 50mVs^{-1}. (d) Frequency curves recorded simultaneously with the cyclic voltammograms shown in (c).

Table1 Electrochemical data of $NH_4P_5W_{30}$ at GCE and gold electrode.

$NH_4P_5W_{30}$	GCE		Gold electrode	
	$E_{1/2}$ (V)	ΔE_p (V)	$E_{1/2}$ (V)	ΔE_p (V)
WO-I/I'	-0.295	0.082	-0.288	0.080
WO-II/II'	-0.420	0.088	-0.416	0.089
WO-III/III'	-0.590	0.051	--	--

Potential (V) *vs* Ag/AgCl and $E_{1/2}=(E_{pa} + E_{pc})/2$ where E_{pc} and E_{pa} are the cathodic and anodic peak potentials. Peak to peak separation, $\Delta E_p=E_{pa} - E_{pc}$.

Table2 Electrochemical data of $(PEI/NH_4P_5W_{30})_8$ multilayer film on GCE and gold electrode in pH2 buffer solution.<W=3>

	GCE				Gold electrode			
	GCE/$(PEI/NH_4P_5W_{30})_8$				Au/MBA/$(PEI/NH_4P_5W_{30})_8$			
Peak	E_{pa} (V)	E_{pc} (V)	$E_{1/2}$ (V)	ΔE_p (V)	E_{pa} (V)	E_{pc} (V)	$E_{1/2}$ (V)	ΔE_p (V)
WO-I/I'	-0.209	-0.226	-0.218	0.017	-0.200	-0.216	-0.208	0.016
WO-II/II'	-0.307	-0.323	-0.315	0.016	-0.312	-0.328	-0.320	0.016
WO-III/III'	-0.384	-0.393	-0.389	0.009	-0.392	-0.398	-0.395	0.006
WO-IV/IV'	-0.432	-0.447	-0.440	0.015	-0.435	-0.451	-0.443	0.016
WO-V/V'	-0.591	-0.606	-0.599	0.015	--	--	--	--

Potential (V) *vs* Ag/AgCl and $E_{1/2}=(E_{pa}+E_{pc})/2$ where E_{pc} and E_{pa} are the cathodic and anodic peak potentials. Peak to peak separation, $\Delta E_p=E_{pa}--E_{pc}$.